Journal of Marine Research, 44, 739–762, 1986

Evolution of the near-surface thermal structure in the western Indian Ocean during FGGE, 1979

by Robert L. Molinari,[1] John Swallow[2] and John F. Festa[1]

ABSTRACT

The evolution of mixed layer temperature (taken as sea-surface temperature, SST) in the western Indian Ocean north of 20S and west of 80E during the First GARP Global Experiment (FGGE), 1979 is described and modelled. The FGGE-year development in time and space of SST is compared to the appropriate climatology. FGGE events occurred in phase with climatology, but some amplitude anomalies were observed. Heat budget computations for the surface mixed layer indicate that over 25% of the region studied energy fluxes through the sea surface can account for 80% of the observed SST variance. South of the equator, 80% of the variance is accounted for in 36% of the area and north, only 11%. Exceptions are noted along the western boundary, in the central and eastern Arabian Sea, and in a band south of the equator between 6S and 12S, east of 60E. The addition of entrainment through the base of the mixed layer improves the heat budget estimates over most of the region, in particular, along the Arabian coast. Near the northern part of the coast of east Africa, however, inclusion of the effect of horizontal advection gives more improvement. The breakdown of the heat budget computations in the central and eastern Arabian Sea and in the band south of the equator is attributed to a small signal in SST variance and few data in the regions.

1. Introduction

The western Indian Ocean, including the Arabian Sea, represents a region of intense air-sea interaction on many time and space scales. As shown by Hastenrath and Lamb (1980), the western Arabian Sea receives a large input of thermal energy through the sea-surface. By as yet undefined mechanisms (Düing and Leetmaa, 1980), this energy is transported to other regions of the oceans to contribute to the maintenance of the global energy balance. On a regional scale, air-sea interaction in the Arabian Sea apparently influences rainfall over the Indian subcontinent (Shukla, 1975, for instance).

Sea-surface temperature (SST) and the heat storage of the surface layer control, in part, the amplitude of the air-sea interaction. The objective of this paper is to describe, through simple models of SST, which processes are important for control of upper

1. National Oceanic and Atmospheric Administration, Atlantic Oceanographic and Meteorological Laboratory, 4301 Rickenbacker Causeway, Miami, Florida, 33149, U.S.A.
2. Heath Cottage, Drakewalls, Gunnislake, Cornwall, England.

layer thermal structure in the western Indian Ocean. Previous studies have shown that the models must include internal oceanic processes as well as energy fluxes through the sea-surface to derive a realistic representation of upper layer thermal history (Düing and Leetmaa, 1980, for instance). This requires a complete suite of near-surface oceanographic observations to evaluate possible effects of horizontal advection and upwelling, for instance.

Synoptic data collected during the First GARP Global Experiment (FGGE) in 1979 are used, supplemented by climatological data whenever necessary. By using synoptic data, phase relations possibly masked by the smoothing inherent in climatologies may be revealed. Although the primary area of interest is the Arabian Sea, the region bounded by 20S, 24N, 40E and 80E (Fig. 1) is considered to include possible boundary effects such as horizontal advection.

In the following sections, the models used to study SST variability are first described. Then the data sources and analysis techniques used to generate mean monthly representations of the relevant surface meteorological and oceanic variables are discussed. Sufficient 1979 data are available on a monthly time-scale to generate basin-wide distributions of SST and surface energy fluxes. These distributions are described in relation to climatological representations of the variables to illustrate the "normalcy" of the 1979 fields. Sufficient FGGE-year data are not available to generate basin-wide, monthly fields of mixed layer depth, MLD, thermocline depth and surface currents. Thus, initial model computations use a combination of FGGE and climatological data as input to depict the basin-wide evolution of the SST fields. This lack of data also precludes any quantitative computations of heat export from the Arabian Sea (as in Düing and Leetmaa, 1980) and of turbulent energy balances in the mixed layer.

A hierarchy of models are considered by adding terms to the heat balance of the mixed layer to determine which processes may dominate in the surface layer dynamics as a function of position in the region. These models generate statistical correlations between observed SST fields and predicted SST fields. Eighteen subregions of the western Indian Ocean are then modelled, using the same hierarchy, to determine if these correlations are physically realizable, to ascertain if the use of climatological data is valid and to illustrate which processes dominate in SST evolution as a function of time.

2. Mixed layer heat budget

The theoretical development of McPhaden (1982), who modelled observations of the surface layer taken at Gan Island (0°41'S, 73°10'E), is followed in order to define which processes control the evolution of the mixed layer temperature (taken as SST) in the western Indian Ocean. The McPhaden (1982) approach as applied here has been used to study larger areas by Molinari *et al.* (1985a).

Following McPhaden (1982), the heat balance of the mixed layer on monthly time

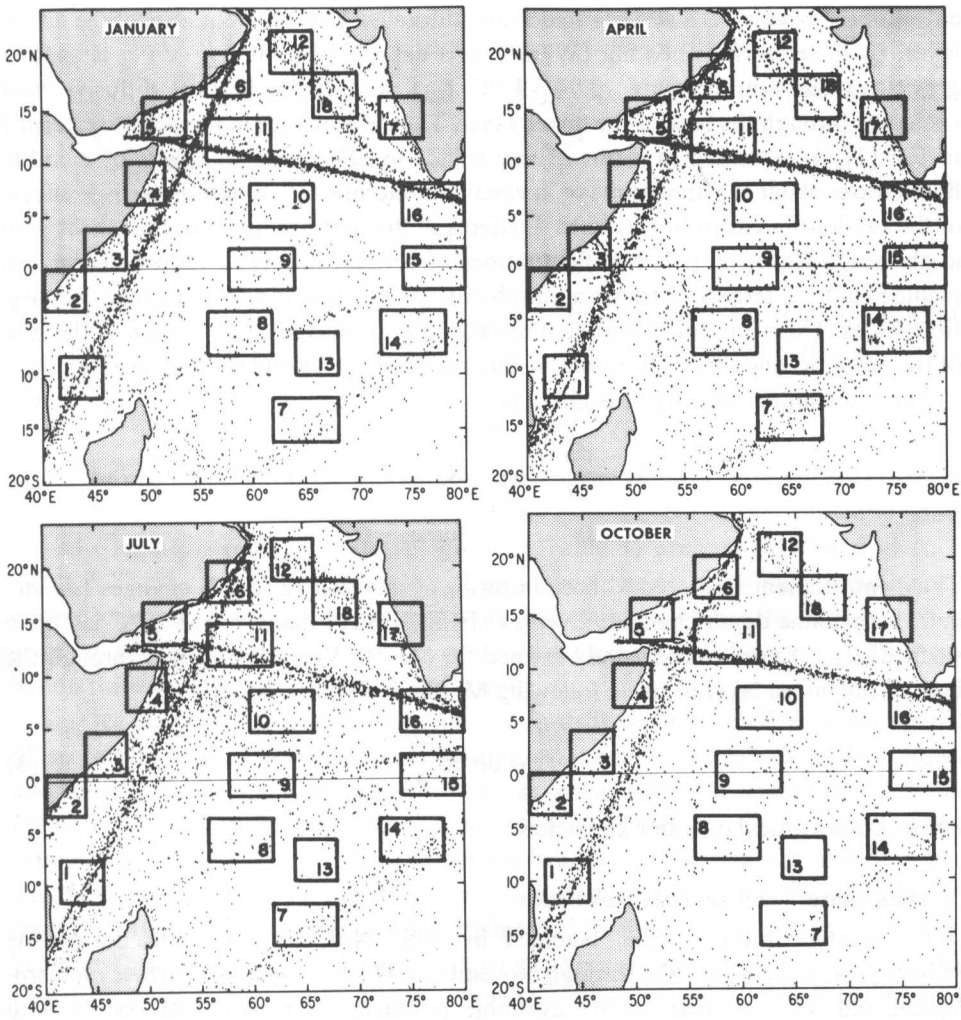

Figure 1. Representative distributions of surface observations. Eighteen subregions discussed in the text are indicated.

scales is expressed as:

$$\underbrace{\frac{\partial T}{\partial t}}_{1} - \frac{1}{\delta T}\underbrace{[T(t_1) - T(t_0)]}_{2} + \underbrace{\left(u\frac{\partial T}{\partial x} + v\frac{\partial T}{\partial y}\right)'}_{3} + \underbrace{\left(\frac{1}{h}\omega_e \Delta T\right)'}_{4} = \frac{1}{\rho c_p}\underbrace{\left(\frac{Q_0}{h}\right)'}_{5} - \underbrace{\left(\frac{Q_{-h}}{h}\right)'}_{6} \qquad (1)$$

where primes denote monthly fluctuations about the annual mean for 1979. The temperature of the mixed layer T is taken as SST, t is time, t_1–t_0 is record length, u is zonal current speed, v is meridional current speed, h is mixed layer depth, ω_e is

entrainment velocity, ΔT is the temperature difference just below the base of the mixed layer, Q_0 is net surface heating (W/m^2), ρ is density (1×10^3 kg/m^3) c_p is specific gravity at constant pressure (3.94 kJ/°C Kg), and Q_{-h} is vertical diffusive heat exchange through the base of the mixed layer. Thus, the change in temperature, term 1 in Eq. (1), is expressed in terms of any trends in SST, term 2; effects of monthly fluctuations about the annual mean in zonal and meridional advection, term 3; effects of fluctuations in entrainment, term 4; effects of fluctuations in net oceanic heat gain at the sea surface, term 5; and fluctuations of vertical diffusion, term 6. Term 2 is included as long-term SST trends are probably not adequately resolved by the one-year time series. The net oceanic heat gain through the sea-surface, Q_0, is given as the sum of the net short and longwave radiation balances and latent and sensible heat fluxes.

The entrainment velocity ω_e is given as

$$\begin{aligned} \omega_e &= \frac{dh}{dt} + \omega_{20} \quad \text{for } \omega_e > 0 \\ &= 0 \qquad\qquad\quad \text{for } \omega_e \leq 0. \end{aligned} \tag{2}$$

Thus, entrainment is expressed both in terms of mixed layer depth changes (dh/dt) and thermocline depth changes, given as changes in the depth of the 20°C isotherm surface (ω_{20}). Entrainment is only defined for $\omega_e > 0$. Vertical diffusion through the base of the mixed layer is given, following McPhaden (1982), as

$$Q_{-h} = \rho c_p K \frac{\partial T}{\partial z} \tag{3}$$

where K is a vertical diffusion coefficient.

3. Data sources and analysis techniques

The western Indian Ocean bounded by 20S, 24N, 40E and 80E during the FGGE-year, December 1978 through November 1979 is considered. Surface meteorological and SST observations are available primarily from merchant vessels, with densest coverage over a few well-travelled shipping lanes (Fig. 1). Subsurface observations are available from merchant vessels which participated in a ship-of-opportunity program (Bruce and Beatty, 1985) and from the research fleet deployed during FGGE. As will be shown, the available subsurface data are much less extensive.

The analysis procedure used by Molinari *et al.* (1985b) is followed to generate surface flux fields. Mean monthly distributions of surface wind, air temperature, cloud cover, specific humidity and SST are generated on a 2° × 2° grid from the FGGE data. Standard error of the mean values are also computed for each quadrangle. Ensemble average estimates for two classes of quadrangles, those within the major shipping lanes and those outside the lanes (Fig. 1) are listed in Table 1. The errors are considerably larger in the data sparse areas.

The mean monthly surface data and the bulk aerodynamic formulas given in

Table 1. Ensemble average standard error of the mean values for quadrangles within the shipping lanes (10–15 values) and outside the shipping lanes (5–10 values).

	10–15 Values	5–10 Values
SST (°C)	.24	.29
Dew point temperature (°C)	.35	.42
Air temperature (°C)	.29	.35
Wind speed (m/s)	.59	.73
Cloud cover (tenths)	.6	.8

Molinari *et al.* (1985b) are then used to estimate the surface latent (Q_E) and sensible (Q_S) heat fluxes, the net shortwave (SW) and longwave (LW) radiation balances and net oceanic heat gain (Q_0),

$$Q_0 = SW - LW - Q_E - Q_S . \tag{4}$$

Using the uncertainty estimates in Table 1 and a propagation of error analysis (Meyer, 1975), error estimates for individual flux terms (as well as for specific humidity which is also computed from the variables given in Table 1) are computed and given in Table 2. These errors are independent of any inadequacies of the bulk formulas and depend only on sampling and instrumental uncertainties. Using the propagation of error analysis, estimated errors in net oceanic heat gain are of the order of 25 W/m^2 within the shipping lanes and 30 W/m^2 outside.

Surface currents are derived from 1979 ship drift reports supplied by the British Meteorological Office. In spite of the limitations inherent in these data, they proved adequate for studying regional current patterns on monthly time scales in the Atlantic (Molinari *et al.*, 1985a). Molinari *et al.* (1985a) suggest errors in these current estimates of about 0.1 m/s. These errors are not strictly random but include a bias depending on wind direction. Subsurface temperature profiles for 1979 were derived from the MOODS data-set of the Fleet Numerical Oceanographic Center. The mixed layer depth is taken as the first depth at which the temperature is 0.5°C less than SST (taken as the first depth of the profile). The thermocline depth is taken as the depth of the 20°C isotherm following Quadfasel (1982). These sources and the years of the data used in deriving the climatologies are listed in Table 3.

Subsurface oceanographic data available during 1979 are limited. Therefore, selected subregions with sufficient data (either synoptic or climatological) to construct the required

Table 2. Ensemble average standard error of the mean values for quadrangles within the shipping lanes (10–15 values) and outside the shipping lanes (5–10 values).

	10–15 Values	5–10 Values
Saturation specific humidity ($g\ Kg^{-1}$)	0.33	0.40
Specific humidity ($g\ Kg^{-1}$)	0.37	0.46
Sensible heat flux (Wm^{-2})	4.2	5.0
Latent heat flux (Wm^{-2})	17.9	21.9
Longwave radiation (Wm^{-2})	3.3	4.4
Shortwave radiation (Wm^{-2})	13.5	18.6

Table 3. Sources of climatological data

Variable	Source	Years of data in climatology
1. Sea-surface temperature	Reynolds (1983)	1854–1976
2. Mixed layer depth/thermocline depth	Molinari *et al.* (1986b)	1948–1981
3. Surface currents	Cutler and Swallow (1984)	1854–1974
4. Surface winds	Hastenrath and Lamb (1979a)	1911–1970
5. Cloud coverage	Hastenrath and Lamb (1979a)	1911–1970
6. Surface energy fluxes	Hastenrath and Lamb (1979b)	1911–1970

annual cycles are studied in more detail. The regions are shown in Figure 1 and provide coverage of many of the distinctive oceanographic features observed in the western Indian Ocean as will be described.

4. Oceanographic and surface energy flux structure

a. Oceanographic conditions

Sea-surface temperature. Mean monthly SST fields for 1979 are shown in Figure 2. The large-scale temperature structure throughout the region during 1979 is very similar to the climatological structure. As the latter structure has been described elsewhere, Hastenrath and Lamb (1979a), hereinafter HL1, for instance, only the large-scale pattern is briefly described here.

In the southern hemisphere, largest SST variability (as given by the variance of the 12-month time series) in the study area is observed south of 10S, east of about 55E (Fig. 3). Large variance is also observed along the entire western boundary, with the exception of a relative minimum on the equator. Much of the variability within the 1.5°C^2 contour in the southern hemisphere can be accounted for by an annual harmonic (Fig. 3) with highest temperatures observed during austral summer and lowest during austral winter (Fig. 2).

North of about 5N along the boundary, the amplitude of the semi-annual harmonic increases (Fig. 3). These are regions of boreal summer coastal upwelling (Fig. 2). Thus, in the western Arabian Sea, there are two cooling seasons, one during boreal winter and one during boreal summer (Fig. 2). In the extreme northeastern Arabian Sea, the large variance is essentially annual in character (Fig. 3). Finally, lowest variances in SST are observed in a region centered on the equator and extending from 6S to 6N east of about 64E. Temperatures within this region are typically greater than 28°C throughout the year with the exception of somewhat lower temperatures during boreal summer (Fig. 2).

As indicated in Table 3, the Reynolds climatology was derived from data collected between 1854 and 1976. Thus, the distributions shown in Figure 2 include an element due to the secular increase in Indian Ocean SST documented by Fieux and Stommel (1976). The 1979 anomalies for their Gulf of Aden to Colombo trackline average

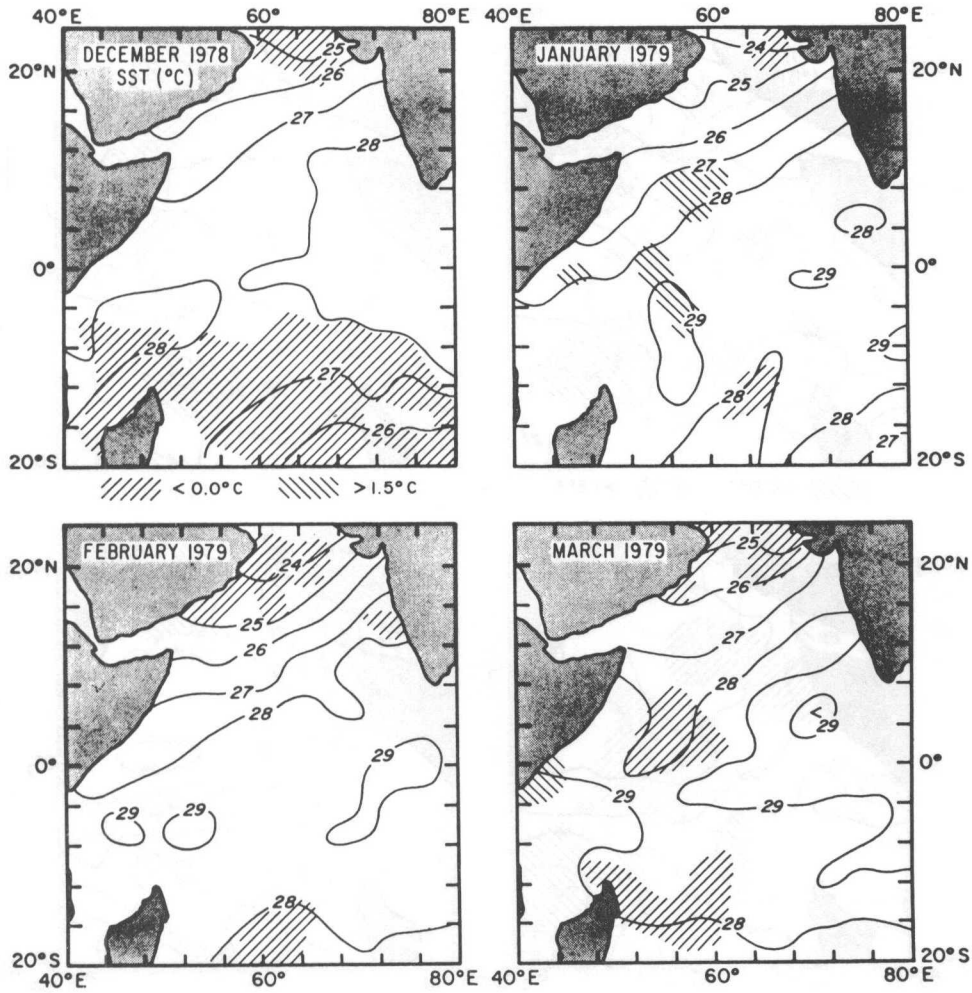

Figure 2. Sea-surface temperature (SST), °C, distributions with SST anomalies, relative to Reynolds (1983), greater than 1.5°C and less than 0°C indicated (see text).

0.8°C. Assuming both that this is a measure of a secular increase relative to the climatological mean for the entire study area for 1979 and that average errors in SST are about 0.3°C (Table 1), only anomalies above and below the sum and difference of these values are significant. Thus, positive anomalies greater than 1.5°C and negative anomalies less than 0°C are indicated on the SST distributions in Figure 2.

An approximately basin-wide belt of negative anomalies occurred during December 1978 between 20S and 5S (Fig. 2). Smaller regions of negative anomaly are observed south of 10S during all other months except November. From July through November, patches of positive anomaly are also observed in this region. The extreme northern Arabian Sea represents another region of persistent anomalies, in this case negative (Fig. 2).

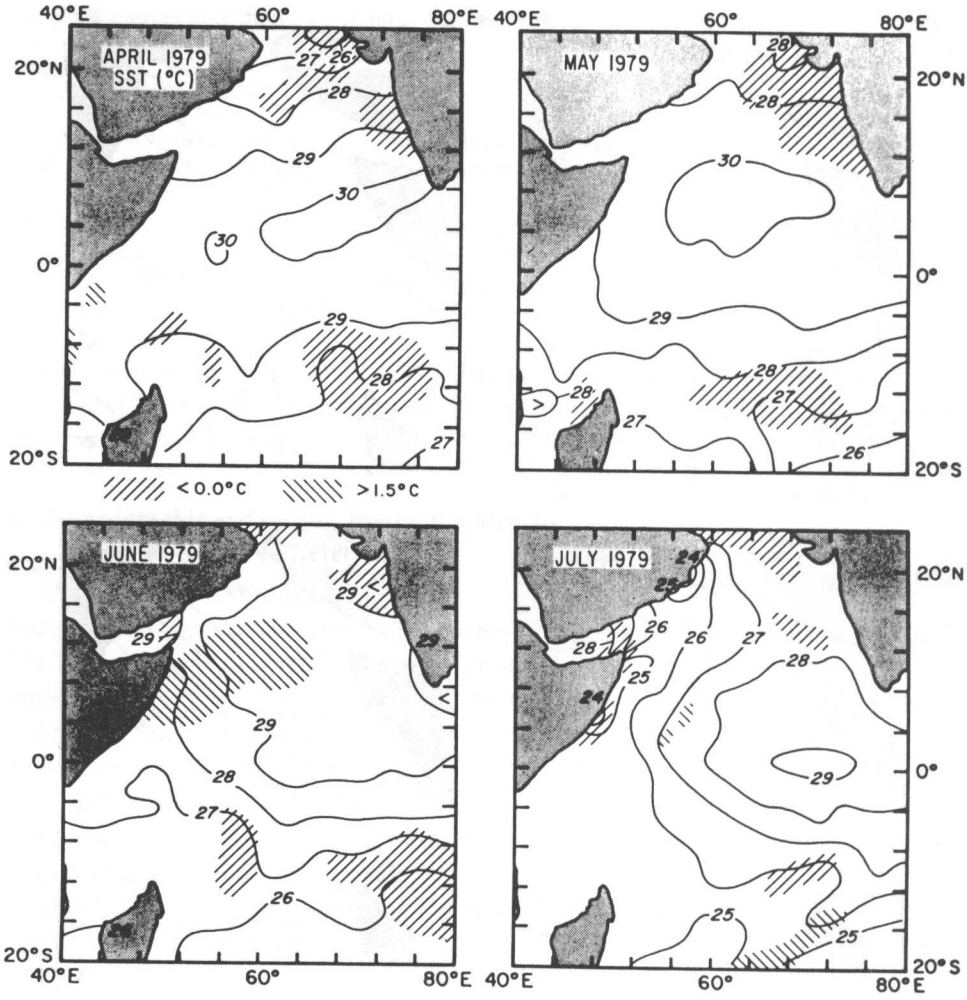

Figure 2. (Continued)

Regions of significant (as defined above) and nearly significant (+1.3°C) positive anomalies appear along the coast near the equator in December and persist through May. In June, a large region of positive anomaly extends from the coast eastward to 65E, between 5N and 10N. The positive anomalies along the coast are replaced by negative anomalies in July extending from 3N to 13N. In August, an almost continuous band of negative anomaly extends along the coast from 23N to 0° and then eastward to 65E between 5S and 0°. Only a small coastal region of negative anomalies centered at 10N appears in September. Finally, two large regions of negative anomaly centered approximately at 0° and 52E are observed in October and November.

Time series of SST for the eighteen subregions are shown in Figure 4. The major events in the 1979 SST time series throughout the basin are in phase with the

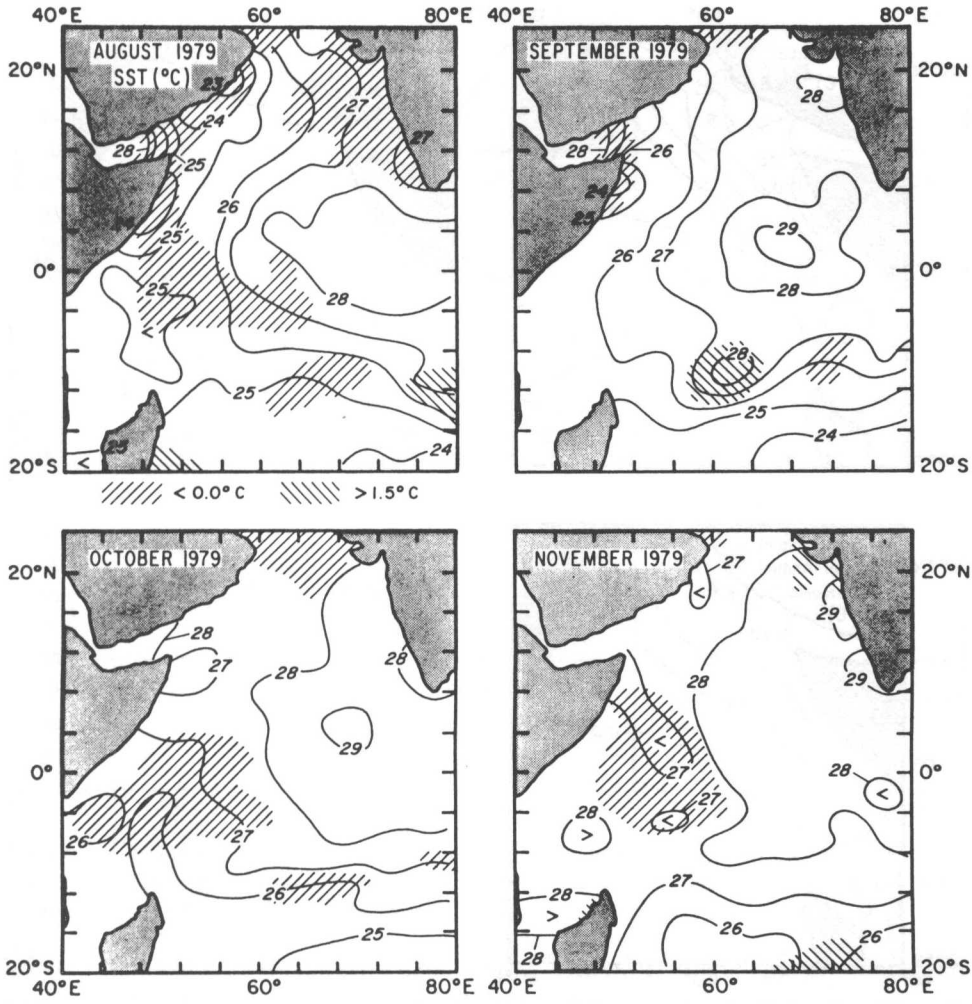

Figure 2. (Continued)

climatological events. Thus, the SST anomalies shown in Figure 3 represent differences in the amplitude of the annual signal rather than in phase.

Mixed layer depth. In addition to climatological monthly mixed layer depth distributions, Molinari *et al.* (1986b), also give the 1979 monthy distributions. Only isolated data are available in December 1978 and January, February and October 1979. When sufficient data are available to generate 1979 distributions by subjective contouring, the 1979 and climatological fields are very similar.

The paucity of subsurface oceanographic data is evident in the gappy and noisy time series of MLD shown in Figure 5. In addition to the 1979 and climatological time series, the MLD panels also give the rms differences between the 1979 and climatological values. For those cases with sufficient data to infer an annual cycle, the 1979 MLD

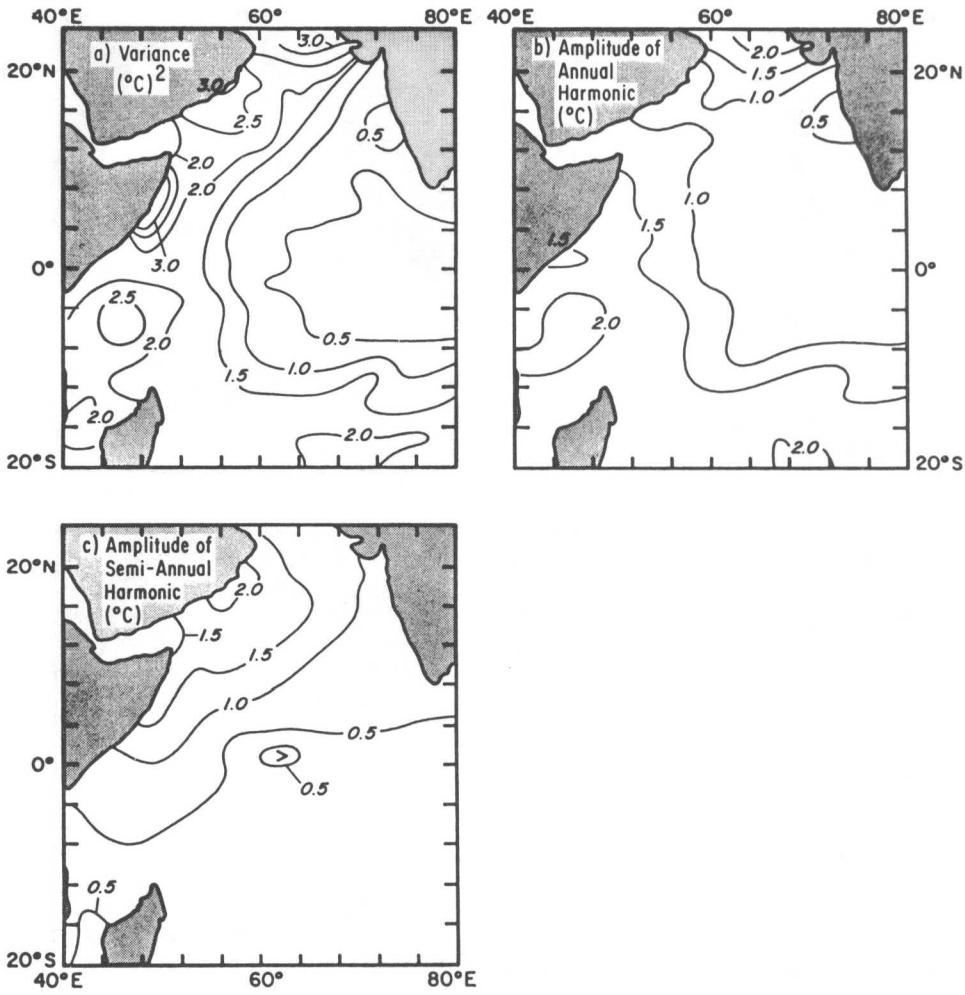

Figure 3. (a) Variance $(°C)^2$ computed from the 1979 mean monthly sea-surface temperature (SST) time series; (b) Amplitude of the annual harmonic computed from the 1979 mean monthly SST time series; (c) Amplitude of the semi-annual harmonic computed from the 1979 mean monthly SST time series.

time series are in phase with the climatological series; e.g., subregions 2, 3, 5, 6, 11, 14, 16 (Fig. 5). There are some instances where anomalies persist over either time or space. For instance, 1979 MLD's were shallower than normal during boreal summer and fall in subregions 3 and 5. However, the anomalies are typically less than 10 m, the vertical resolution available from the observed temperature profiles (i.e., the differences are within observational uncertainties).

Thermocline depth. The 1979 thermocline data are somewhat noisier than the MLD data (Fig. 5). However, as in the case with MLD's, when an annual cycle can be

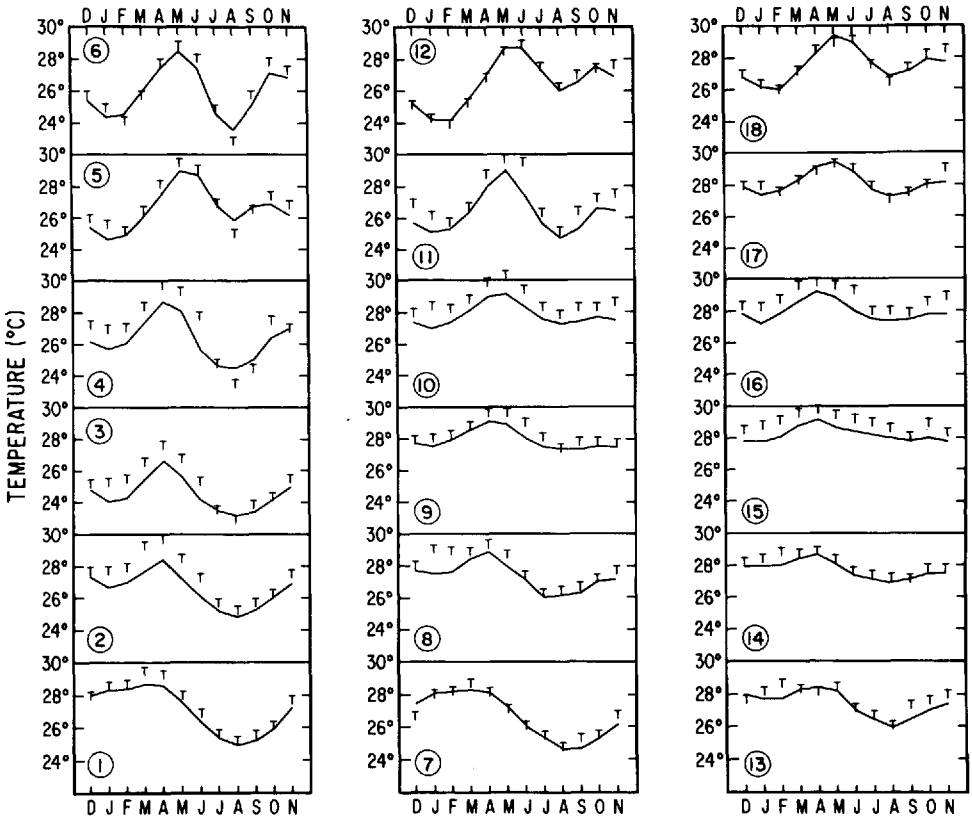

Figure 4. Comparison between nearly monthly 1979 sea-surface temperatures (denoted by T) and climatological sea-surface temperature (from Reynolds [1983] and given by the solid line) for the eighteen subregions shown in Figure 1.

inferred from the 1979 thermocline data, it is in phase with climatology. Because of the paucity of data in time and space it is difficult to discern any persistent anomalies in thermocline depth. In general, however, the majority of the anomalies are less than 10 m. In summary, using climatological MLD's will not, within observational errors, introduce systematic errors into the heat balance estimates. However, thermocline differences, through entrainment may effect heat balance estimates. Although the data are too noisy to quantify this effect, qualitative estimates of the impact of these differences on the heat budget computations will be made.

Surface currents. Systematic differences between 1979 and climatological surface current distribution are apparent in Figure 6. For instance, in the south central Indian Ocean (subregions 8 and 9), throughout the year there is anomalously higher westward flow, while in subregions 10 and 11, similar anomalies occur after May (Fig. 6). Similarly, along the entire boundary anomalously higher northward flow occurs from January through March, with a suggestion of predominantly southward anomalies

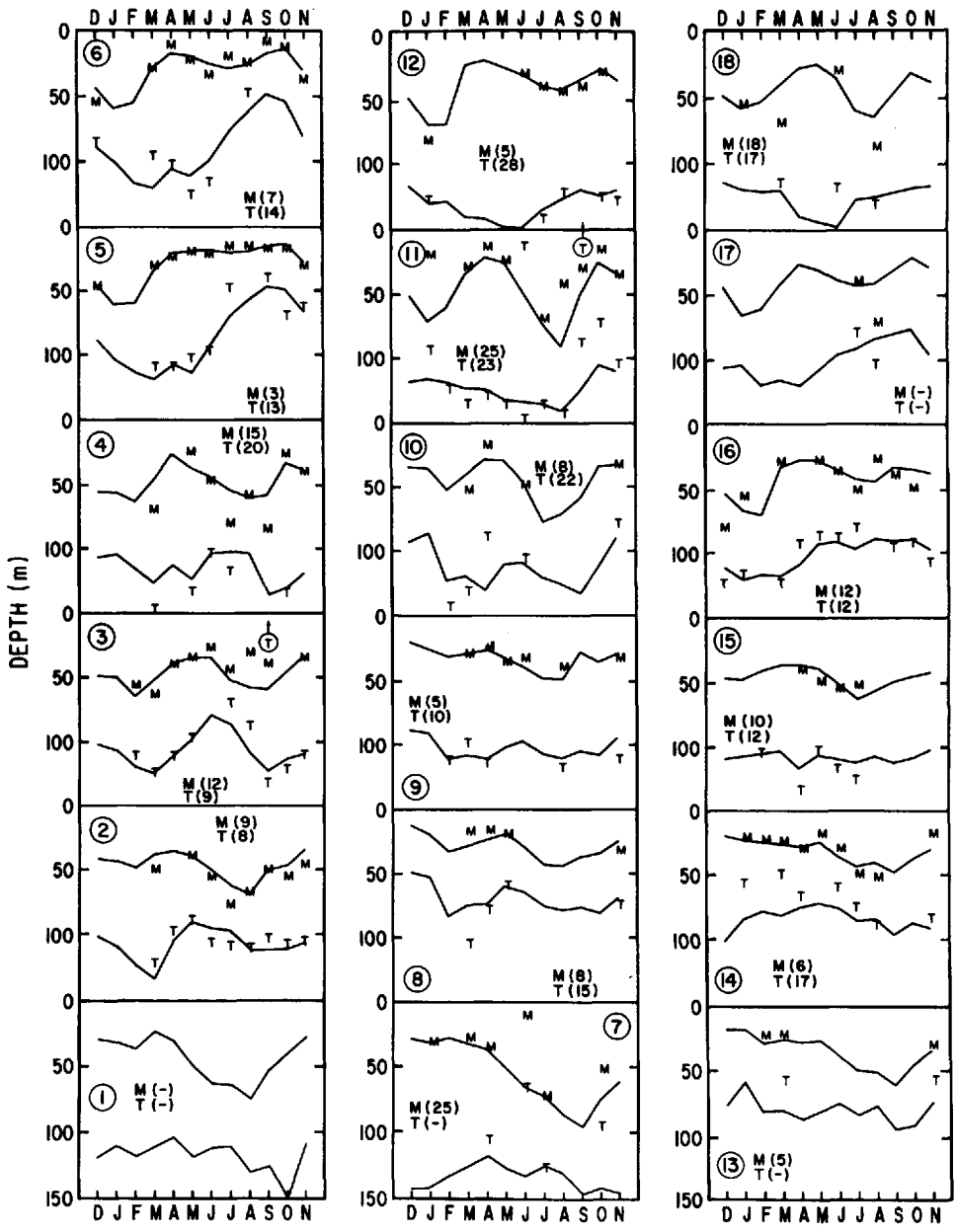

Figure 5. Comparison between mean monthly 1979 mixed layer depths (denoted by M) and thermocline depths (denoted by T) and climatological mixed layer and thermocline depths (from Molinari *et al.* [1986b] and denoted by solid lines) for the eighteen subregions shown in Figure 1. RMS differences between the two time series, in m, are given.

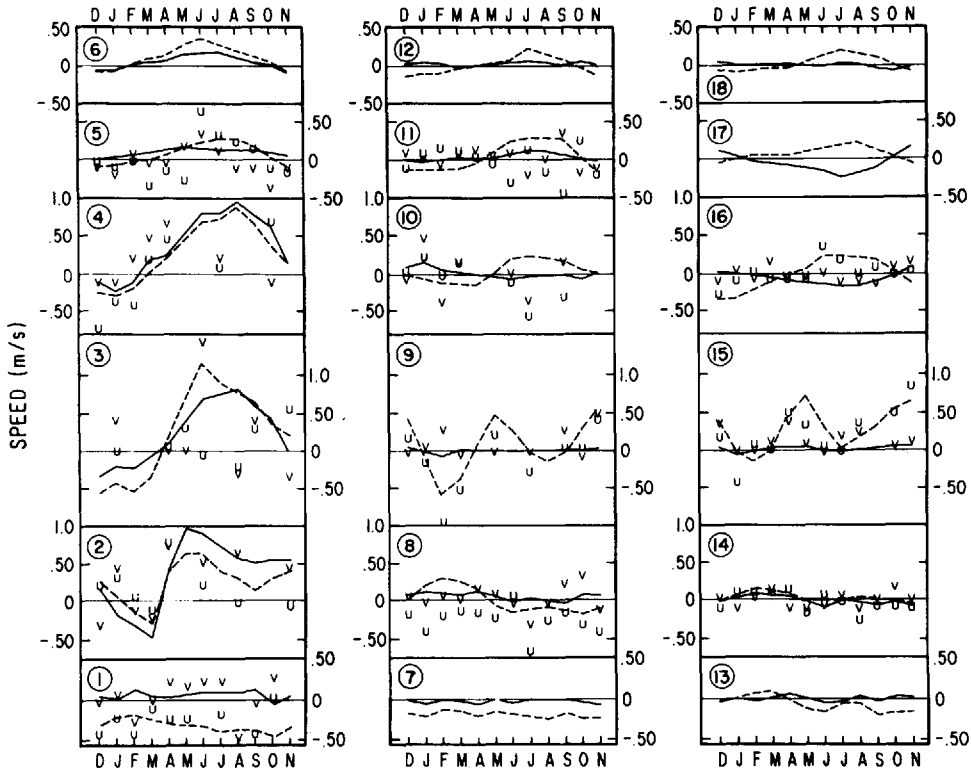

Figure 6. Comparison between mean monthly 1979 u-components of surface current (denoted by u) and v-components of surface current (denoted by v) and climatological currents (from Cutler and Swallow [1984]; u-component given by dashed line and v-component by solid line) for the eighteen subregions shown in Figure 1.

throughout the remainder of the year. These anomalies must be considered qualitatively rather than quantitatively because of the paucity of data.

b. Surface energy fluxes

The 1979 mean monthly distributions of net long and shortwave radiation balances and latent and sensible heat fluxes are given in Molinari *et al.* (1986a). The meteorological fields used to generate the surface flux fields are also given there. The 1979 mean annual distributions of three of these variables are shown in Figure 6. The longwave radiation distribution is not shown because the field is very flat with only the 60 W/m^2 contour appearing. The appropriate contours from Hastenrath and Lamb (1979b), hereinafter HL2, are also given.

The large-scale patterns of these energy fluxes observed during 1979 are very similar to the climatological patterns both on the monthly time scales shown in Molinari *et al.* (1986a) and the annual time scale shown in Figure 7. For instance, the latent heat

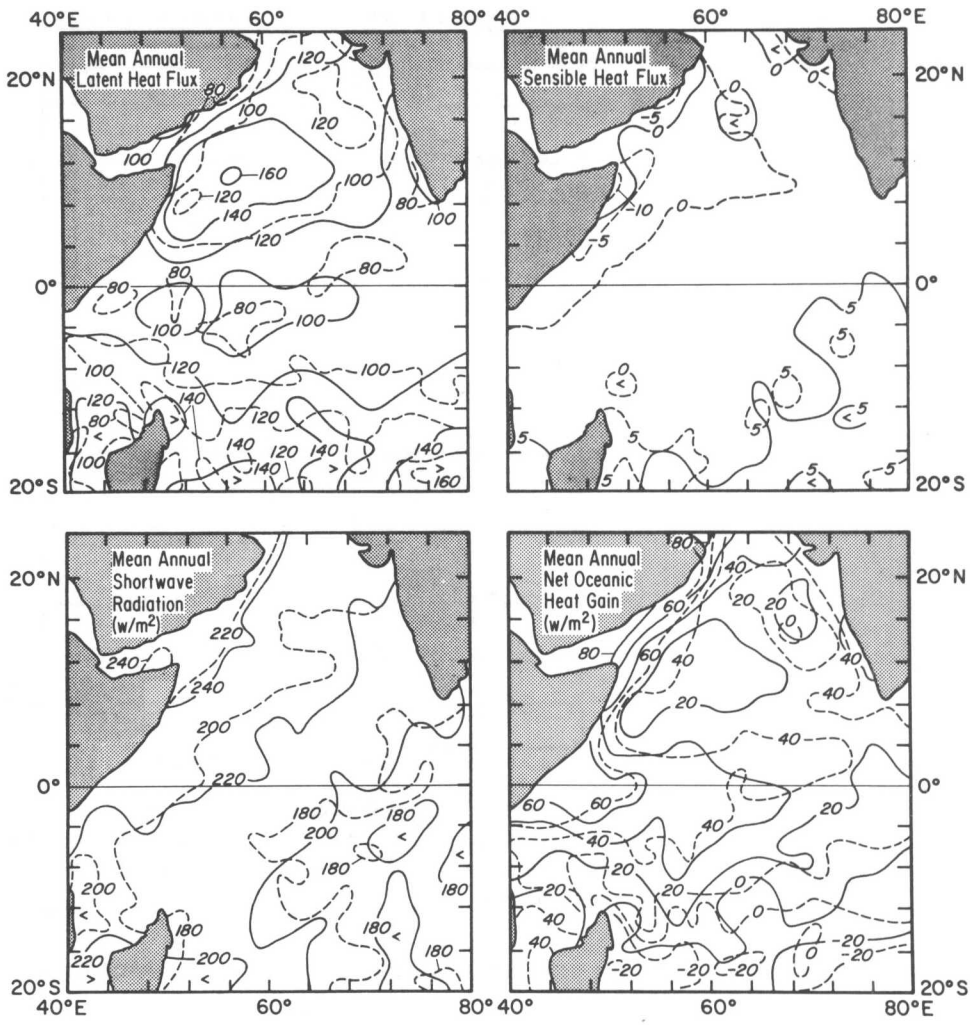

Figure 7. Mean annual distributions in W/m^2 for 1979 of latent and sensible heat fluxes, net short radiation balances and net oceanic heat gain. Dashed lines are from Hastenrath and Lamb (1979b).

distributions are characterized by a maximum in the southern portion of the region, under the southeast Trades and another maximum off Somalia, under the boreal summer, Findlater Jet. The shortwave radiation balances during 1979 are also similar to the climatology, decreasing from a maximum in the northwest corner of the grid to a minimum in the southeast. The flat spatial structure in the annual sensible heat and longwave radiation balances (not shown) reflect similar patterns in the mean monthly patterns.

The mean annual net oceanic heat gain distribution for 1979 is also shown in Fig-

ure 7. Both on the annual time-scale and the monthly time scales shown in Molinari *et al.* (1986a), the 1979 patterns are very similar to the climatological patterns given in HL2. In particular, the relative minima in heat gain in the Arabian Sea is due to two seasons of heat loss, boreal winter and summer (as will be shown shortly), coincident with the maxima in monsoonal winds. In the southern hemisphere, the minimum in heat gain (Fig. 7) lies under the Southeast Trades. Here, maximum heat loss occurs during boreal summer when the Trades are the strongest (Molinari *et al.*, 1986a).

As surface fluxes are strongly dependent on wind speed, time series of wind speed as well as net surface oceanic heat gain are given in Figure 8 for the 18 subregions. To compare the 1979 and climatological values, the climatological range within the subregion of the variable (from HL1 or HL2) is given. The coincidence in both hemispheres of the high surface fluxes and winds as described in the preceding paragraph is clear. For instance, in subregions 11 and 12, there is net surface cooling during both monsoons (Fig. 8). Net surface cooling occurs in the southern hemisphere subregions (1, 2, 7, 8, 13, 14) during boreal summer. In both cases, there are no significant and/or persistent anomalies in either phase or amplitude (Fig. 8). Thus, in terms of surface forcing, within the monthly 2° × 2° resolution used in this study, 1979 was a "normal" year. These results are, in general, consistent with those of Luther *et al.* (1985) who discussed FGGE winds from March through October.

5. Mixed layer modelling results

The heat balance expressed in (1) can be tested using a combination of historical and 1979 data. Historical data are required to provide the necessary oceanographic input on a 2° × 2° monthly grid. The 1979 data provide SST and surface forcing input. The integration of (1) using (3) yields

$$T_E(t) = T(t_2) + \frac{1}{\delta t}\left[T(t_1) - T(t_0)\right](t - t_2) - \int_{t_2}^{t}\left[\left(u\frac{\partial T}{\partial x}\right)' + \left(v\frac{\partial T}{\partial y}\right)'\right]dt \qquad (3)$$

$$- \frac{1}{\rho c_p}\int_{t_2}^{t}\left(\frac{1}{h}\omega_e \Delta T\right)'dt + \frac{1}{\rho c_p}\int_{t_2}^{t}\left(\frac{Q_0}{h}\right)'dt - \int_{t_2}^{t}\left(\frac{K}{h}\frac{\partial T}{\partial z}\right)'dt \qquad (5)$$

(4) (5) (6)

where T_E represents an estimated mixed layer temperature. The *arbitrary* constant of integration $T(t_2)$ is chosen such that the mean of the estimated time series is equal to the mean of the observed time series. Thus, the integration (prediction) does not necessarily begin on the initial value of the observed time series, but can begin on any value of the record. To repeat McPhaden (1982), this heat balance "predicts fluctuations and not actual values of mixed layer temperature."

A hierarchy of models is developed, first considering term 5 alone and then adding terms 3, 4 and 6. As a quantitative measure of the *statistical* relationship between the

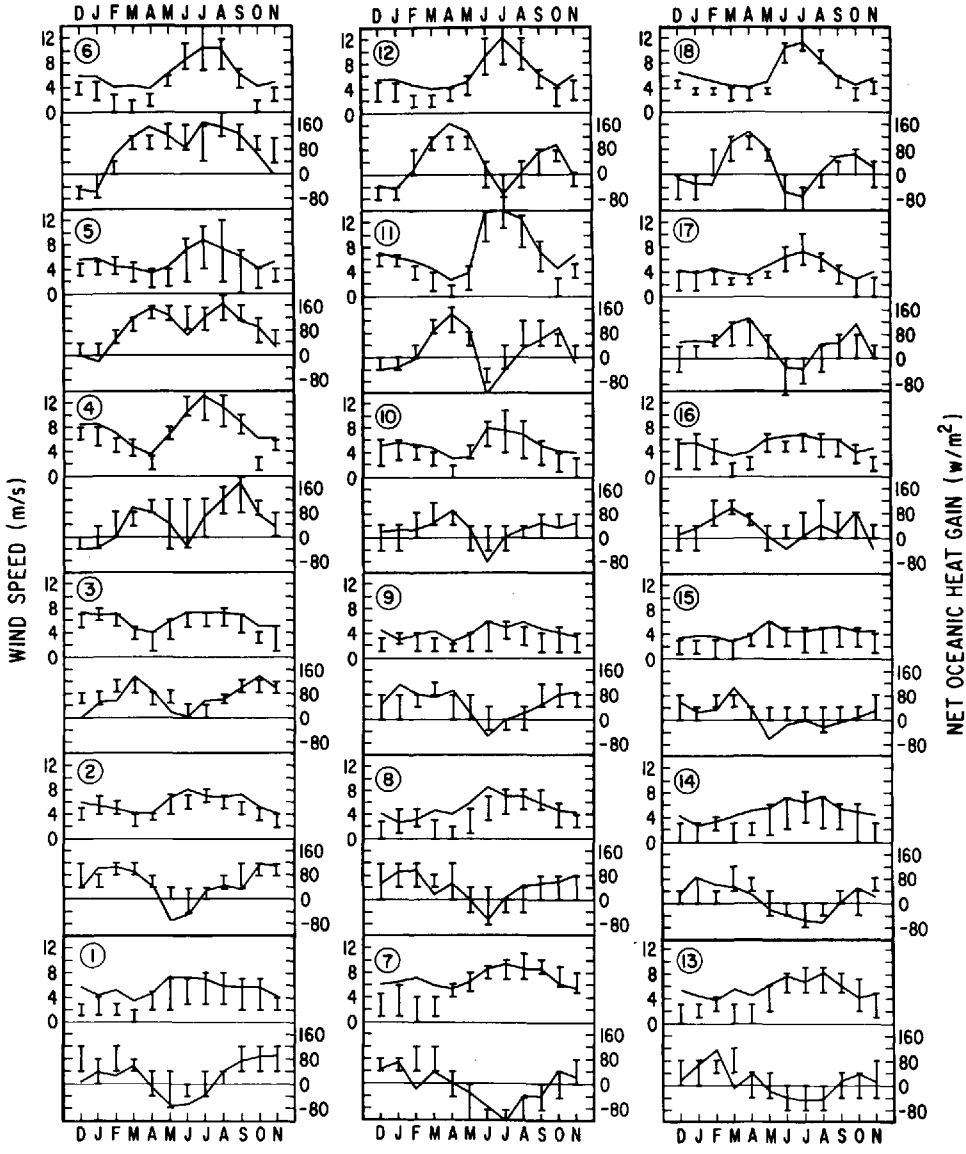

Figure 8. Comparison between mean monthly 1979 surface wind speeds (solid lines) and net oceanic heat gain (solid lines) and climatological wind speeds from Hastenrath and Lamb (1979a) and heat gain from Hastenrath and Lamb (1979b). Bars indicate the range of each variable in the selected subregion as determined from the appropriate climatology.

estimates of SST and observations, a linear correlation coefficient is used

$$r^2 = \frac{[\Sigma(T_0\, T_E)]^2}{[\Sigma(T_0)^2]\,[\Sigma(T_E)^2]}. \tag{6}$$

The observed, T_0, and estimated, T_E, temperatures have zero means. In the first model, values of Q_0 are obtained from the 1979 data and values of h from the climatological data. As in McPhaden (1982), the correlation coefficient also represents the percentage of variance in the original time series accounted for by the estimated time series. The resulting distribution of correlation coefficients is shown in Figure 9.

The correlation coefficient is greater than 0.6 over large portions of the region. In fact, correlations greater than 0.8 are computed for 25% of the area studied (36% south and 11% north of the equator). Distinctly lower coefficients occur in four regions. Along the coastal upwelling regions where SST variances are large (Fig. 3), correlations are less than 0.2. Correlations less than 0.6 extend offshore from the western boundary to 72E in a band between about 4N and 14N. Another band of correlations less than 0.6 extends from the eastern boundary to 56E between about 14S and 4S, a region of sparse data coverage (Fig. 1). Finally, another region of lower correlations occurs south of India. In the last two regions, total SST variance is small, generally less than $1°C^2$.

Correlation coefficients derived from Eq. (5) as written are also shown in Figure 9. The vertical distribution of currents in the mixed layer is unknown except for a few isolated regions along the western boundary (Leetmaa *et al.*, 1982). It is somewhat arbitrarily assumed that average mixed layer velocities are one-half the value determined from the ship-drift reports. A series of simulations was attempted in which different reductions of surface speeds, as given by the ship drift reports, were used to estimate average mixed layer currents. On the average, a 50% reduction in surface speeds produced the greatest improvement in the correlations. A vertical diffusion coefficient of $.1 \times 10^{-4}$ m^2/s is assumed. A basinwide average vertical temperature gradient at the base of the mixed layer of 1°C/10 m was somewhat arbitrarily used during all months except June, July, August and September. An enhanced gradient of 3°C/10 m was used during these summer months. Changes in these diffusion variables had a negligible effect on the overall heat budget.

Improvements in the correlation coefficients are particularly dramatic in the Arabian Sea. Here, where variances are high (Fig. 3), correlations less than 0.6 now only occur along the African and Arabian coasts. For comparison with the surface flux model, it is noted that coefficients greater than 0.8 are computed for 45% of the region studied (56% south of 0° and 30% north). Isolated regions of low correlation occur in the eastern Arabian Sea where variances are less than $0.5°C^2$ (Fig. 3). Although not as extensive, improvements in the correlations are also observed in the southeastern portion of the basin (Fig. 9).

The correlations given in Figure 9 represent *statistical* measures of possible

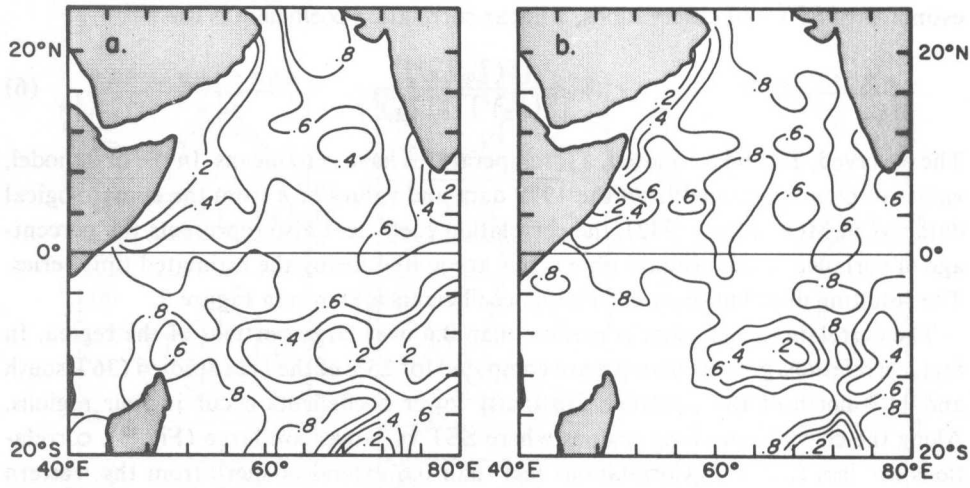

Figure 9. Correlation coefficients (Eq. 6) between observed temperatures and temperatures estimated from surface fluxes only, left panel and from surface fluxes, entrainment, horizontal advection and vertical diffusion, right panel.

relationships between observed and estimated temperatures. Further analysis is required to determine if these statistical correlations are *physically* consistent with observations of mixed layer structure. In addition, the significance of the estimates of the four processes must be addressed in view of both observational uncertainties and possible differences between the climatological conditions (when used to derive SST estimates) and the actual 1979 conditions.

The physical consistency of the correlations given in Figure 9 is addressed by describing time series of observed and predicted mixed layer temperature series for the eighteen subregions of Figure 1. Since we employ a centered difference formulation for the advection terms, we can only estimate the effects of this process in subregions surrounded by data points. Along the boundary, estimates of advective effects from these points are considered representative of the entire subregion.

For brevity, the nomenclature given in Table 4 is used for the discussion of model results. The results from the model applications are summarized in Table 5. Both correlation coefficients and rms differences between observed and estimated time series are listed for all the subregions. The high correlations in many areas of the basin derived from Model 1 (Fig. 9) are physically consistent in that the time series of observed and estimated SST are similar in both phase and amplitude (Fig. 10). In particular, correlation coefficients are greater than 0.80 along the boundary south of the equator (subregions 1 and 2, Table 5) where the annual signal dominates in the SST time series. High correlations also are obtained in the eastern Arabian Sea (subregions 17 and 18). The low correlations (<0.80) south of the equator in subregions of few data (8, 13 and 14) are characterized by sharper extrema in the

Table 4. Model applications.

Model number	Processes [terms in Eq. (6)]
1	Surface fluxes (5)
2	Surface fluxes, entrainment (4, 5)
3	Surface fluxes, entrainment, horizontal advection (3, 4, 5)
4	Surface fluxes, entrainment, horizontal advection, vertical diffusion (3, 4, 5, 6)

predicted time series than in the observed time series (Fig. 10). In the central subregions north of the equator (subregions 10 and 11) surface fluxes also contribute to the semi-annual signal in SST (i.e., surface fluxes contribute to the boreal summer cooling). However, north of the equator along the boundary in subregions 4, 5 and 6, surfaces fluxes contribute to boreal winter cooling but do not cause boreal summer cooling. Furthermore, the amplitudes of the modelled winter cooling and spring warming are considerably larger than the observed events.

Entrainment improves the predictions most dramatically along the boundary, north of the equator. Here, as shown by the results from Model 2 in Figure 10, entrainment increases boreal summer cooling in subregions 3 and 4 and causes boreal summer cooling in subregions 5 and 6. Warming occurred in summer in 5 and 6 when Model 1 was applied. However, the winter and spring discrepancies between the observed and estimated SST's apparent in the results from Model 1 still persist.

Table 5. Correlation coefficient/rms difference between observed and predicted monthly SST changes for the eighteen subregions shown in Figure 1 and the four models listed in Table 4.

Subregion	Model 1	Model 2	Model 3	Model 4
1	.97/0.27	.97/0.28	.96/0.33	.95/0.38
2	.92/0.42	.90/0.79	.78/1.37	.78/1.40
3	.57/0.97	.83/0.61	.43/0.97	.46/0.95
4	.00/2.00	.05/1.89	.81/0.79	.81/0.79
5	.00/3.49	.08/2.30	.01/3.06	.01/2.98
6	.08/2.85	.20/2.36	.32/2.09	.31/2.10
7	.61/0.82	.88/0.46	.90/0.46	.91/0.42
8	.78/1.03	.87/1.06	.93/0.80	.93/0.80
9	.85/1.00	.83/1.12	.89/0.83	.89/0.78
10	.82/0.36	.93/0.22	.95/0.32	.95/0.31
11	.52/1.10	.64/0.98	.60/0.98	.60/0.98
12	.88/1.49	.93/1.50	.94/1.49	.95/1.48
13	.22/1.28	.41/1.37	.36/1.41	.37/1.34
14	.58/1.47	.78/1.06	.83/0.81	.85/0.79
15	.75/0.50	.78/0.67	.76/0.51	.76/0.51
16	.35/0.65	.72/0.42	.71/0.47	.72/0.49
17	.77/0.50	.91/0.62	.93/0.58	.93/0.60
18	.71/0.73	.87/0.65	.86/0.75	.86/0.76

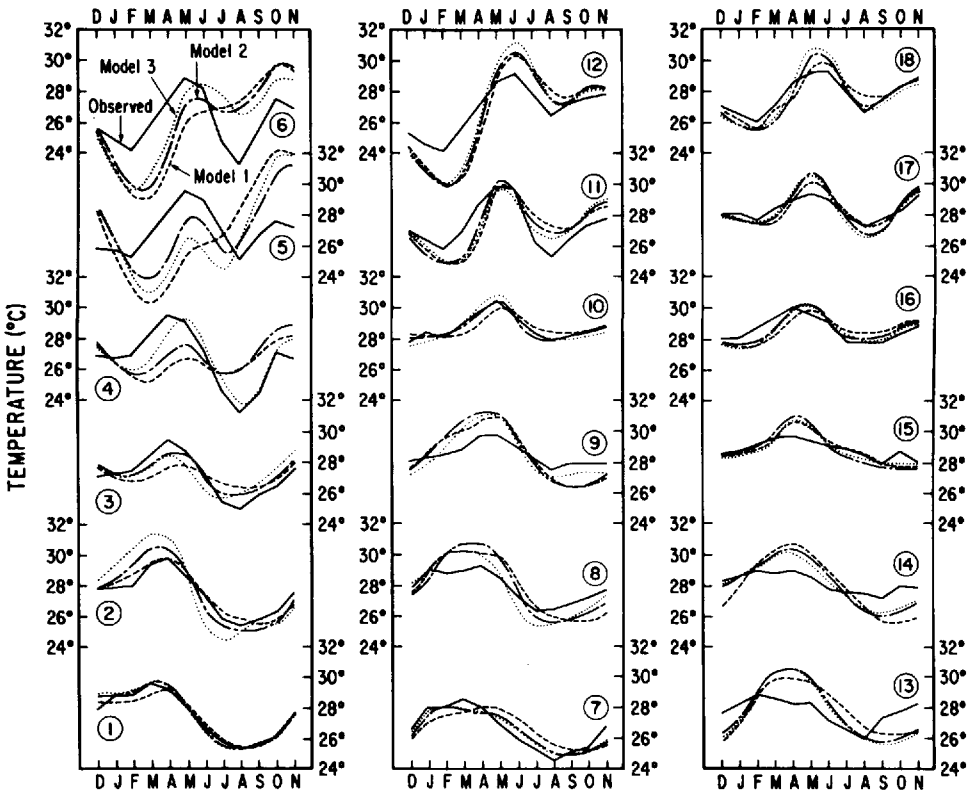

Figure 10. Observed temperature time series and temperature time series estimated from Models 1, 2 and 3 (Table 4) for the eighteen subregions shown in Figure 1.

The results from the application of Model 3 are also shown in Figure 10. When sufficient data are available to construct an annual cycle for 1979 surface currents and the resulting annual cycle is dramatically different from climatology (Fig. 6), the 1979 data are used in the predictions. Advective effects are typically small throughout the basin (Fig. 10 and Table 5). Largest advective effects occur along the boundary (subregions 4 and 6) and south of the equator (subregions 11 and 14). In some subregions, advection degrades the predictions (subregions 2 and 5, for instance). Possible reasons for this degradation are offered shortly. Diffusive effects are not shown in Figure 10, but are listed in Table 5. The differences between Models 3 and 4 are negligible. Model 4 was rerun using a K of 1×10^{-4} m^2/s and the predictions were in general degraded throughout the region.

The significance of the correlation coefficients and reductions in rms differences is now considered by estimating errors introduced into the computations by observational uncertainties and differences between the 1979 and climatological variables. Errors in net oceanic heat gain are of the order of 25 W/m^2 along the shipping lanes and

Table 6. Ensemble average properties for the eighteen subregions shown in Figure 1 and uncertainty estimates for each variable.

Property	Average	Uncertainty
Mixed layer depth (m)	42	10
Thermocline depth (m)	107	10
Absolute value of zonal speed (m/s)	0.18	0.10
Absolute value of meridional speed (m/s)	0.07	0.10
Absolute value of zonal temperature gradient (°C/m)	8.74×10^{-7}	6.43×10^{-7}
Absolute value of meridional temperature gradient (°C/m)	12.23×10^{-7}	6.43×10^{-7}
Net oceanic heat gain (W/m^2)	26	35
Entrainment (m/s)	16.03×10^{-7}	54.56×10^{-7}
Temperature difference at base of mixed layer (°C)	2.42	0.5

30 W/m^2 outside the lanes (Table 2). The lower error estimate is equivalent to an uncertainty in temperature change over one month of about 0.6°C for a 25 m MLD, 0.3°C for a 50 m MLD and 0.2°C for a 75 m MLD. Inverting the problem, differences between observed and predicted temperature changes in a region of high correlation can be used to obtain another estimate of heat gain error. In subregion 2, the average difference between observed and predicted monthly temperature changes is 0.48°C and the average MLD is 43 m. These values equate to an uncertainty in net oceanic heat gain of 32 W/m^2, similar to the errors derived from Table 2.

Using a propagation of error analysis (Meyer, 1975), errors introduced into the model computations by observational uncertainties are estimated. Based on previous discussions, measurement errors of 30 W/m^2 in surface flux, 10 m in mixed layer and thermocline depths, 0.25 in SST and .1 m/s in surface currents are assumed. Comparisons of 1979 and climatological MLD and thermocline depths (Fig. 5) indicate that differences are generally within the observational uncertainties. As stated previously, 1979 currents are used when differences from climatology are large.

Error estimates are derived assuming that the processes modelled are independent. For each subregion the average properties needed for the error computation are determined and then ensemble averages are computed (Table 6). Using these averages and the uncertainty estimates listed in the same table, expected errors in monthly temperature changes for each of the processes considered in Eq. (5) are estimated. The average error (on a monthly time-scale) associated with uncertainties in surface fluxes and mixed layer depths [term 5, Eq. (5)] is 0.46°C; entrainment, temperature differences at the base of the mixed layer and mixed layer depths [term 4, Eq. (5)] is 0.82°C; and zonal and meridional speeds and temperature gradients [term 3, Eq. (5)] is 0.62°C. Diffuse errors are 0.02°C. It should be stressed that these represent average errors to be expected. There are spatial structures to the error distributions. For

instance, because speeds and temperature gradients are larger along the boundary, advective errors are also larger.

6. Discussion

Throughout most of the study area, correlations between observed temperatures and temperatures predicted from the surface flux model are high (Figs. 9 and 10). The surface flux model breaks down north of the equator along the western boundary, in a band extending from the eastern boundary between 12S and 6S and in isolated regions in the eastern Arabian Sea (Fig. 9). Along the western boundary, the discrepancies between observed and estimated time series can be characterized as follows: In subregions 3 and 4, the amplitude of the estimated time series is less than the amplitude of the observed time series (Fig. 10). In subregions 5 and 6, the amplitude of estimated time series is larger than the observed amplitude and only boreal winter cooling is predicted.

The uncertainty in estimates of monthly temperature change associated with entrainment is 0.82°C. Based on this uncertainty estimate, the addition of entrainment to surface fluxes in Model 2 only improves the predictions (as given by rms differences between observed and predicted temperature changes) in subregion 5. Here, Model 2 rms differences are 1.19°C less than Model 1 differences (Table 5). Although not significant in view of the uncertainties in estimates of entrainment, a relatively large reduction in rms differences is also realized in subregion 6 (0.49°C, Table 5). The improvement in the predictions is related to entrainment driven summer cooling in both subregions, a feature not found in the results of Model 1 (Fig. 10). Entrainment also improves the predictions in subregions 3 and 4 by increasing summer cooling, but not significantly.

The current regime in subregions 3 and 4 is characterized by the seasonally reversing Somali Current and the spin-up of two gyres during boreal summer (Swallow *et al.*, 1983). During summer, the currents of the southern gyre separate from the coast between 2N and 5N. The currents of the northern gyre, the so-called "Great Whirl" separate between 7N and 10N. Upwelling is observed coincident with both separation zones. The introduction of advection in Model 3 only improves the predictions significantly (i.e., greater than the 0.62°C uncertainty in advective effects) in subregion 4, the northwestern portion of the Great Whirl. Here advection increases the amplitude of the summer cooling (Fig. 10), in line with the observations. However, advection frequently degrades the predictions along the boundary such as in subregions 2, 3 and 6. This degradation is probably indicative of the crude manner in which advection is parameterized in a region of complicated vertical velocity structure (Leetmaa *et al.*, 1982) and intense horizontal temperature gradients (Evans and Brown, 1981). Although not significant in view of the error estimates, predictions are improved by including advection in the subregions on and south of the equator (subregions 8, 9, and 14, Table 5). The equatorial subregions include the seasonally

reversing Wyrtki Jet (Wyrtki, 1973) indicated by the dramatic changes in zonal velocity component shown in Figure 6.

The band of low correlations between about 14S and 4S and 65E and 80E (Fig. 9) is coincident with a region of sparse data coverage throughout the year (Fig. 1). Total variances in the monthly SST time series are less than 1.5°C^2 in this area (Fig. 3). The combination of low signal amplitude and large noise due to few data is the probable cause of the low correlations. In fact, the band of low correlations is broken by a region of higher correlations (Fig. 9) along a shipping lane (Fig. 1). The correlations are higher in subregion 14 which includes the shipping lane than in subregion 13 which does not (Fig. 1).

Although isolated regions of low correlation occur in the eastern portions of the Arabian Sea (Fig. 9), they typically are coincident with total SST variances less than 0.5°C^2 (Fig. 3). Again the low correlations are probably indicative of a low signal-to-noise ratio in these regions as hypothesized for the region south of the equator.

In summary, these results emphasize the need to include energy fluxes through the sea surface when modelling the temperature of the mixed layer. Away from the boundaries and in regions with adequate data to define the important processes surface fluxes can account for a significant portion of the variance in time series of mixed layer temperature.

Along the western boundary oceanic processes are important and entrainment improves significantly (in terms of uncertainties in the computations) the predictions along the Arabian coastline. Similarly, horizontal advection improves the predictions along the northern African coastline. Vertical diffusion using a reasonable diffusion coefficient has a minor effect on the predictions. There are significant anomalies in 1979 SST distributions relative to climatology. However, results of this study are inadequate to quantify their cause. Future studies should concentrate on the parameterizations of the various processes along the boundaries and ways to increase the data coverage in presently data void areas with the goal of defining the causes of observed anomalies.

Acknowledgments. This effort was supported in part by the NOAA Office of Climate Research.

REFERENCES

Bruce, J. G. and W. H. Beatty. 1985. Some observations of the coalescing of Somali eddies and a description of the Socotra eddy. Oceanologica Acta, *8,* 207–219.

Cutler, A. N. and J. C. Swallow. 1984. Surface currents of the Indian Ocean (to 25S, 100E): Compiled from historical data archived by the Meteorological Office, Bracknell, UK. Institute of Oceanographic Sciences Report, No. 187, 8 pp. and 36 charts.

Düing, W. and A. Leetmaa. 1980. Arabian Sea cooling: A preliminary heat budget. J. Phys. Oceanogr., *10,* 307–312.

Evans, R. H. and O. B. Brown. 1981. Propagation of thermal fronts in the Somali Current system. Deep-Sea Res., *28A,* 521–527.

Fieux, M. and H. Stommel. 1976. Sea-surface temperatures in the Arabian Sea. Ann. Inst. Oceanogr. Paris, *52*,5–15.

Hastenrath, S. and P. J. Lamb. 1979a. Climatic Atlas of the Indian Ocean. Part I: Surface Climate and Atmospheric Circulation. The University of Wisconsin Press, Madison, WI, 19 pp., 97 charts.

—— 1979b. Climatic Atlas of the Indian Ocean. Part II: The Oceanic Heat Budget. The University of Wisconsin Press, Madison, WI, 93 pp.

—— 1980. On the heat budget of hydrosphere and atmosphere in the Indian Ocean. J. Phys. Oceanogr., *10*, 694–708.

Leetmaa, A., D. R. Quadfasel and D. Wilson. 1982. Development of the flow field during the onset of the Somali Current, 1979. J. Phys. Oceanogr., *12*, 1325–1342.

Luther, M. E., J. J. O'Brien and A. M. Meng. 1985. Morphology of the Somali Current system during the southwest monsoon, *in* Coupled Ocean Atmosphere Models, J. C. J. Nihoul, ed., Elsevier Press, Amsterdam, 405–437.

McPhaden, M. J. 1982. Variability in the central equatorial Indian Ocean, Part II: Oceanic heat and turbulent energy balances. J. Mar. Res., *40*, 403–419.

Meyer, S. L. 1975. Data Analyses for Scientists and Engineers. John Wiley, New York, 513 pp.

Molinari, R. L., J. F. Festa and E. Marmolejo. 1985a. Evolution of sea-surface temperature in the tropical Atlantic Ocean during FGGE, 1979: II. Oceanographic fields and heat balance of the mixed layer. J. Mar. Res., *43*, 67–81.

—— 1985b. Evolution of sea-surface temperature and surface meteorological fields in the tropical Atlantic Ocean during FGGE 1979. Prog. in Oceanogr., *14*, 401–420.

—— 1986a. Heat budget and climatic atlas of the tropical western Indian Ocean during FGGE (1979). NOAA Tech. Memo. ERL AOML-63, 76 pp.

Molinari, R. L., J. F. Festa and J. C. Swallow. 1986b. Mixed layer and thermocline climatologies in the western Indian Ocean. To appear as a NOAA Tech. Memo.

Quadfasel, D. R. 1982. Low-frequency variability of the 20°C isotherm topography in the western equatorial Indian Ocean. J. Geophys. Res., *87*, 1990–1996.

Reynolds, R. W. 1983. A comparison of sea surface temperature anomalies. J. Clim. Appl. Met., *22*, 447–459.

Shukla, J. 1975. Effect of Arabian Sea surface temperature anomaly on Indian summer monsoon. A numerical experiment with the GFDL model. J. Atm. Sci., *32*, 503–511.

Swallow, J. C., R. L. Molinari, J. G. Bruce, O. B. Brown and R. H. Evans. 1983. Development of near-surface flow pattern and water mass distribution in the Somali Basin, in response to the southwest monsoon of 1979. J. Phys. Oceanogr., *13*, 1398–1415.

Wyrtki, K. 1973. An equatorial jet in the Indian Ocean. Science, *181*, 262–264.

Received: *2 April, 1986*; revised: *16 July, 1986.*